Chemical Science

ROYAL SOCIETY
OF CHEMISTRY

EDGE ARTICLE
Zongyou Yin, Yaping Du *et al.*
Lanthanide doping induced electrochemical enhancement
of Na₂Ti₃O₇ anodes for sodium-ion batteries

EDGE ARTICLE

Check for updates

Lanthanide doping induced electrochemical enhancement of Na₂Ti₃O₇ anodes for sodium-ion batteries†

Jiale Xia,‡[a] Hongyang Zhao,‡[ab] Wei Kong Pang, [c] Zongyou Yin, *[d] Bo Zhou,[e] Gang He, [a] Zaiping Guo [c] and Yaping Du [*af]

Na₂Ti₃O₇ is considered as a promising anode material for sodium ion batteries (SIBs) due to its excellent high-rate performance compared with hard carbons. However, the electrochemical performance of Na₂Ti₃O₇ is heavily limited by its low electrical conductivity. In this study, we synthesized a series of lanthanide (Ln = La, Ce, Nd, Sm, Gd, Er, and Yb) doped microsized Na₂Ti₃O₇ anode materials and systematically studied the electrochemical performance. Compared with pristine Na₂Ti₃O₇, all the doped samples show superior electrochemical performance. Especially, the Yb^{3+} doped sample not only delivers a high reversible capacity of 89.4 mA h g^{-1} at 30C, but also maintains 71.6 mA h g^{-1} at 5C after 1600 cycles, nearly twice that of pristine Na₂Ti₃O₇. It is found for the first time that the enhancement in doped samples is attributed to the introduction of lanthanides which induces lattice distortion and oxygen vacancies.

Introduction

Insertion-type electrodes are always the first choice for battery electrodes because alkali metal ions can repeatedly intercalate into the layers of electrode materials without destroying their crystal lattices which will occur in transition-type and alloy-type electrodes.[1–4] The excellent performance of insertion-type electrodes can be interpreted as being due to intercalation pseudocapacitance, in which the capacity is independent of rate in an appropriate current range.[5] Therefore, insertion-type electrodes usually have excellent cycle life and good rate capability. However, limited kinds of materials can be used for anodes for insertion-type sodium ion batteries (SIBs). Materials with excellent rate performance in lithium ion batteries (LIBs) cannot maintain their performance when used for SIBs due to the larger ionic radius of sodium.

ᵃFrontier Institute of Science and Technology, Xi'an Jiaotong University, 99 Yanxiang Road, Yanta District, Xi'an, Shaanxi, 710054, China. E-mail: ypdu@nankai.edu.cn

ᵇSchool of Science, Xi'an Jiaotong University, 28 Xianning West Road, Xi'an, Shaanxi, 710049, China

ᶜInstitute for Superconducting and Electronic Materials, University of Wollongong, 2522 NSW, Australia

ᵈResearch School of Chemistry, The Australian National University, Canberra, Australian Capital Territory 2601, Australia. E-mail: zongyou.yin@anu.edu.au

ᵉDepartment of Physics, Northwest University, Shaanxi, 710069, China

ᶠSchool of Materials Science and Engineering, National Institute for Advanced Materials, Nankai University, 38 Tongyan Road, Haihe Education Park, Tianjin 300350, China

† Electronic supplementary information (ESI) available. See DOI: 10.1039/c7sc05185a

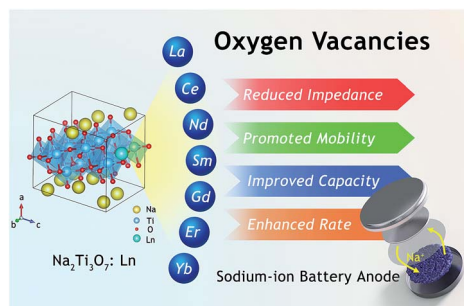‡ These authors contributed equally.

Na₂Ti₃O₇ (NTO) is a promising insertion-type anode material because the TiO₆ octahedron layer can reversibly accommodate sodium ions during cycling, with a theoretical capacity of 178 mA h g^{-1}.[6] Besides, NTO has an efficient low charge–discharge plateau of 0.3 V and is the first ever reported oxide to reversibly react with sodium at such a low voltage.[7] However, the low electrical conductivity makes it difficult to reach its theoretical capacity and the specific capacity of NTO is quite low compared with those of hard carbons or even some organic anodes.[8–10] In addition, the fast capacity fading during long-time cycling has greatly limited its practical application for SIBs.[11] Based on the above concerns, there is an urgent need to find a way to enhance the intrinsic electrical conductivity of NTO.

It is reported that creating defects in the crystal lattice can enhance the conductivity as well as the capacity of metal oxide electrodes.[12–15] As an important kind of dopant in LIB electrodes, lanthanide ions can significantly enhance both the capacity and rate performance of the electrodes.[16–18] Even a trace amount of lanthanide introduction would lead to a great enhancement of specific capacity as well as rate performance of LIBs. This inspired us to transplant such a doping strategy from LIBs to SIBs. To date, lanthanide doped electrodes for SIBs, especially insertion-type anode materials, have never been reported. In order to systematically study the doping effect, we used microsized NTO to eliminate the contribution of surface redox reactions. La, Ce, Nd, Sm, Gd, Er and Yb as representatives of light, middle and heavy lanthanides were chosen as dopants and introduced into NTO (labeled NTO:Ln).

Compared with pristine NTO, the doped samples show superior electrochemical performance. Especially, NTO:Yb not only delivers a high reversible capacity of 89.4 mA h g^{-1} at 30C,

Fig. 1 Schematic illustration of the lanthanide doped $Na_2Ti_3O_7$ anode for SIBs.

but also maintains 71.6 mA h g^{-1} at 5C after 1600 cycles, nearly twice that of pristine NTO. Therefore, NTO:Yb is selected as a representative to illustrate the effects of doping a lanthanide on the structure and the electrochemical performance of NTO. It is found for the first time that the electrochemical enhancement in doped samples could be attributed to the introduction of lanthanides, which induces lattice distortion and oxygen defects, resulting in improved electrical conductivity and charge storage kinetics (Fig. 1).

Results and discussion

The electrochemical performance is evaluated between 0.01 and 2.5 V. It can be observed that both NTO and NTO:Yb have low voltage plateaus at 0.3 V (Fig. 2a and b), which are consistent with the CV measurements (Fig. S1, ESI†). The voltage plateaus of both NTO and NTO:Yb gradually disappear in the following charge/discharge process which may be attributed to the

reconstructed crystal structure during the sodium intercalation or the electrode polarization.[19,20] However, after 1000 cycles, there is still a small voltage plateau of NTO:Yb while the plateau of NTO almost disappeared, suggesting that doping Yb^{3+} could stabilize the electrode structure during the charge/discharge process, thereby leading to a better rate performance of NTO:Yb, which will be further discussed later.

The initial discharge capacity of NTO is 214.1 mA h g^{-1} at the current rate of 1C and then decreases to a mere 44.9 mA h g^{-1} at the highest current rate of 30C. In the meantime, NTO:Yb delivers a much better rate performance with the delivered capacity being 89.4 mA h g^{-1} at 30C, almost twice as much as the capacity of NTO (Fig. 2c). Additionally, when the current rate returns back to 1C after a high rate cycling at 30C, the capacity of NTO:Yb increases to 153.1 mA h g^{-1} with 60.02% retention of the initial capacity, while the capacity of NTO recovered to only 96.4 mA h g^{-1} with a capacity retention of 45.03%. After 1500 cycles at 5C, the discharge capacity of NTO is 43.9 mA h g^{-1} with a capacity retention of 34.58%, but for NTO:Yb, the discharge capacity remains at 71.6 mA h g^{-1} with a capacity retention of 46.02% (Fig. 2d). The capacities of both NTO and NTO:Yb decline rapidly after several cycles at 5C, and the irreversible capacity loss could be attributed to the increasing polarization caused by the electrolyte decomposition or side reaction and the formation of a solid electrolyte interface (SEI) layer.[11,20]

To further analyze the kinetics of NTO and NTO:Yb at different rates, we calculate the b-values of the materials through the analysis of CV plots (Fig. S2, ESI†). In a CV scan, the current i is a function of the scan rate v through the following relationship:[21]

$$i = av^b \tag{1}$$
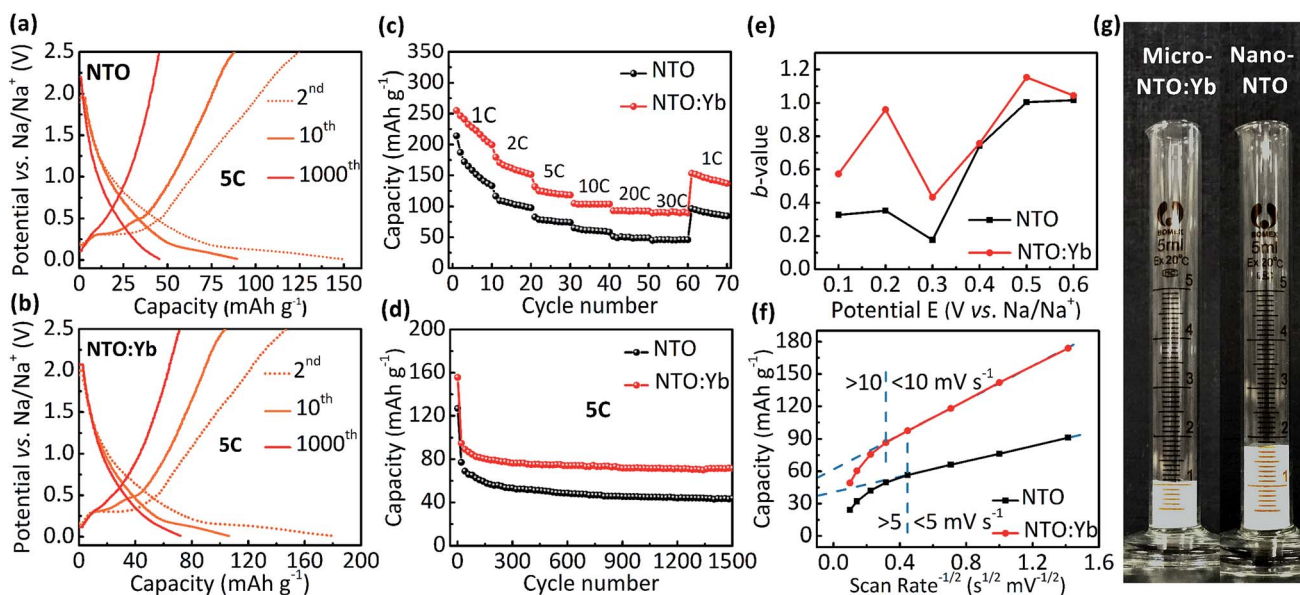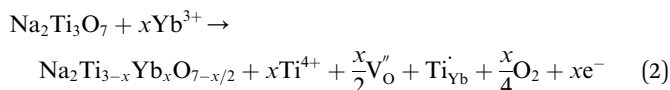

Fig. 2 The 2nd, 10th, and 1000th charge/discharge curves of (a) NTO and (b) NTO:Yb. (c) The rate and (d) cycle performance of NTO and NTO:Yb in a half cell. (e) b-values for NTO and NTO:Yb as a function of potential for anodic sweeps (Na$^+$ insertion). (f) Capacity versus $v^{-1/2}$ allows for the separation of diffusion-controlled capacity from capacitive-controlled capacity. (g) The comparison of tap densities of nano-NTO and micro-NTO:Yb.

where a and b are both adjustable parameters. When the b-value approaches 0.5, the electrode shows diffusion controlled kinetics dominated by the faradaic current, while when the b-value approaches 1, the electrode shows surface controlled kinetics dominated by the capacitive current.[22] The b-values of NTO:Yb are remarkably higher than those of NTO at each voltage (Fig. 2e). This explains the better rate performance of NTO:Yb. The b-values for both samples show a decrease around 0.3 V, corresponding to the position of the main redox peaks. The relationship between the capacity and the square root of the scan rate illustrates the rate-limiting step of the charge storage mechanism (Fig. 2f).[23] For the NTO electrode, in region 1, where the scan rate is below 5 mV s^{-1}, the capacity is mostly independent of the scan rate. In region 2, from 5 to 100 mV s^{-1}, the capacity decreases linearly with $v^{-1/2}$, indicating that the diffusion reaction takes control of the charge storage process at a high scan rate. That is, when the scan rate is larger than 5 mV s^{-1}, diffusion is rate limiting and the pristine NTO electrode stops behaving like a pseudocapacitor and starts behaving like a traditional battery. However, for the NTO:Yb electrode, it can behave in a fully capacitive manner at the scan rate of 10 mV s^{-1} or lower,[24] which means a better rate performance of NTO:Yb at relatively low rates. Electrochemical impedance spectra (EIS) measurements are also performed in the frequency range from 100 to 0.01 kHz (Fig. S3, ESI†). The charge transfer resistance of NTO decreases after doping Yb^{3+}. Moreover, NTO shows diffusion controlled kinetics while NTO:Yb more likely shows a pseudo-capacitive behavior, which is consistent with the b-value analysis. It should be noted that the tap density of micro-sized NTO:Yb is about 0.91 g cm^{-3} while that of nano-sized NTO is 0.55 g cm^{-3} (Fig. 2g), indicating that the volumetric capacity of NTO:Yb (139 mA h cm^{-3} at 1C) is much higher than those of widely reported nanosized NTO powders and approaches closer to its theoretical volumetric capacity (307 mA h cm^{-3}). Besides, the higher volumetric capacity of microsized NTO:Yb is also beneficial to its potential commercialization.

The microstructures of NTO and NTO:Yb are further elucidated by HRTEM and Rietveld XRD refinement (Fig. S4, ESI†). It is clearly demonstrated that the obtained lattice parameters of a, b and c decrease after Yb^{3+} doping, and the tiny shrink of the lattice distance may attribute to the stronger bonding energy of the Yb–O bond. It is believed that the crystal lattice distortion owing to the introduction of lanthanide ions will give rise to the generation of oxygen vacancies.[25] The reaction for oxygen vacancy formation using Kroger–Vink notation can be expressed as:

$$Na_2Ti_3O_7 + xYb^{3+} \rightarrow$$
$$Na_2Ti_{3-x}Yb_xO_{7-x/2} + xTi^{4+} + \frac{x}{2}V_O^{''} + Ti_{Yb}^{\cdot} + \frac{x}{4}O_2 + xe^- \quad (2)$$

As oxygen vacancies can act as shallow donors and thereby increase the carrier density as well as the electrical conductivity,[26] the improved electrochemical performance can be attributed to the formation of oxygen vacancies, and comprehensive studies are carried out to illustrate the existence and effects of oxygen vacancies.

Furthermore, X-ray photoelectron spectroscopy (XPS) shows additional peaks corresponding to Ti 2p doublets of Ti^{3+} at 457.7 and 463.6 eV in NTO:Yb, suggesting that there is a small quantity of Ti ion reduced from Ti^{4+} to Ti^{3+} to maintain the charge compensation (Fig. 3a and b).[27] These results indicate that doping Yb^{3+} into the structure of NTO causes the generation of oxygen vacancies, leading to partial reduction of the Ti element as well as the increasing number of unlocalized electrons, which will improve the electrical conductivity and show better electrochemical performance of NTO:Yb.

Thermogravimetric analysis (TGA) is employed to provide a greater insight into the oxygen vacancies in both NTO and NTO:Yb.[28] The larger mass discrepancies of NTO:Yb between air and N$_2$ suggest a larger oxygen vacancy concentration (Fig. S5, ESI†), which is consistent with the results of XPS analysis. The electrical conductivity is investigated by EIS and a four-probe test. The bulk conductivity of NTO is calculated to be 1.188×10^{-7} S cm^{-1}, which is lower than the value of NTO:Yb at 1.888×10^{-7} S cm^{-1} (Fig. 3c). Besides, the conductivities obtained by the four probe method (Table S1, ESI†) agree with the results of EIS, indicating a better electron transport in the bulk of Yb^{3+} doped materials, corresponding to the better rate performance of NTO:Yb.

In addition, Mott–Schottky (M–S) analysis is also employed to calculate donor densities. It can be obviously observed that NTO:Yb delivers a larger donor density than NTO owing to the lower slope in the M–S plots (Fig. 3d), and the values of donor densities are calculated to be 3.5292×10^{26} and $11.1549 \times$
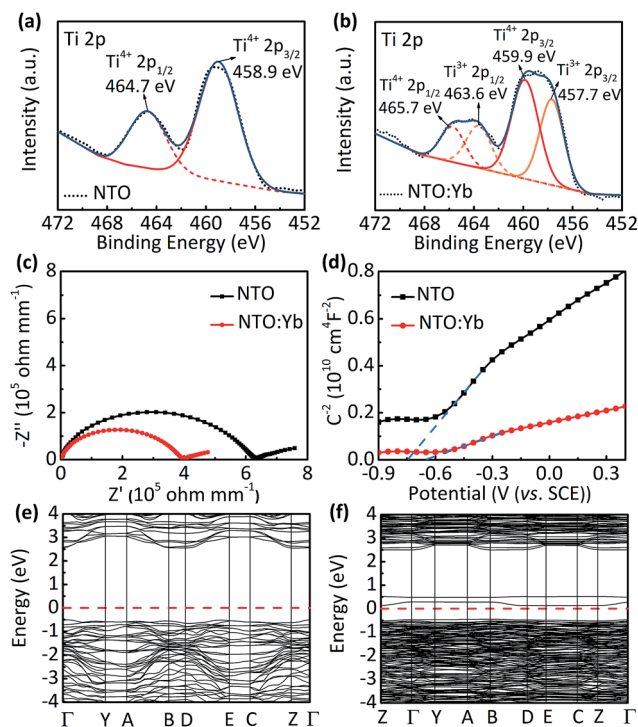

Fig. 3 The Ti 2p XPS spectra of (a) NTO and (b) NTO:Yb. (c) EIS at room temperature of the pellets made from NTO and NTO:Yb for the bulk conductivity measurement. (d) The Mott−Schottky plots of NTO and NTO:Yb at the frequency of 500 Hz. The calculated band structure in the irreducible Brillouin zone of (e) NTO and (f) NTO:Yb.

Fig. 4 (a) The powder XRD patterns of NTO and NTO:Ln (Ln = La, Ce, Nd, Sm, Gd, Er, and Yb). (b) The cyclic performance of NTO and NTO:Ln at the current rate of 5C with the number of cycles ranging from 1000 to 1500. (c) The overview of capacities, electron conductivities and donor densities of NTO and NTO:Ln.

10^{26} cm^{-3} for NTO and NTO:Yb, respectively. The improvement of electron conductivity and donor densities after doping Yb^{3+} can be ascribed to the increasing oxygen vacancies.

First principles calculations are carried out to obtain further insight into the electronic conductivity change of NTO:Yb. The Yb^{3+} doped Na$_2$Ti$_3$O$_7$ system is modeled by substituting one of the 18 Ti ions with a Yb ion (Fig. S6, ESI†). The band structure and density of states (DOS) of NTO and NTO:Yb which can initially describe the intrinsic characterization of electronic conductivity are presented in Fig. 3e and f and S7 (ESI†).[26] It can be seen that NTO shows a direct bandgap of 3.07 eV while the bandgap of NTO:Yb decreased to 0.58 eV, which indicates that the polaron migration energy barrier along the constrained pathway is decreased,[25] thus attributing to a larger electronic conductivity of NTO:Yb.

Finally, we have an overview of structure and electrochemical performance of all NTO:Ln samples. The major diffraction peaks of XRD patterns of all samples match well with the standard XRD trace of Na$_2$Ti$_3$O$_7$ (JCPDS no. 31-1329) (Fig. 4a). The existence of Ti^{3+} as well as other Ln^{3+} ions is confirmed by XPS (Fig. S8 and S9, ESI†). Besides, all samples are micro-sized materials (Fig. S10, ESI†). The rate and long-term cycling performances (Fig. 4b, S11 and S12, ESI†) show that all the Ln^{3+} doped samples exhibited better electrochemical performance than NTO. Among all these electrodes, NTO:Yb presented the best performance, followed by NTO:Er, NTO:Gd, NTO:La, NTO:Ce, NTO:Sm and NTO:Nd successively. Importantly, it's clear that the capacity as well as the conductivity and donor density of each sample are in a sort order (Fig. 4c, S13 and Table S2, ESI†), which is well consistent with the concentrations of oxygen vacancies of each sample (Fig. S14, ESI†).

Conclusions

In summary, we have synthesized for the first time a series of lanthanide doped NTO electrode materials through a high-temperature solid-state method. All the lanthanide doped NTO samples exhibited superior electrochemical performance to pristine NTO. For the first time, we have achieved high performance for NTO anodes without nanosizing and carbon-coating. The introduction of lanthanide into the structure of NTO leads to a slight lattice distortion, thus giving rise to the generation of oxygen vacancies, which significantly improves the electronic conductivity and donor density of NTO and promotes faster charge storage kinetics, thereby ensuring a superior rate performance and long-time cycle performance. We believe that the incorporation of lanthanides into insertion-type electrode materials could provide a new avenue for constructing anode materials with excellent electrochemical performance for large-scale energy storage.

Conflicts of interest

There are no conflicts to declare.

Acknowledgements

Notes and references

1 J. M. Tarascon and M. Armand, *Nature*, 2001, **414**, 359–367.
2 V. Aravindan, J. Gnanaraj, Y. S. Lee and S. Madhavi, *Chem. Rev.*, 2014, **114**, 11619–11635.
3 L. Shen, S. Chen, J. Maier and Y. Yu, *Adv. Mater.*, 2017, **29**, 1701571.
4 L. Shen, E. Uchaker, X. Zhang and G. Cao, *Adv. Mater.*, 2012, **24**, 6502–6506.
5 V. Augustyn, P. Simon and B. Dunn, *Energy Environ. Sci.*, 2014, **7**, 1597.
6 S. Dong, L. Shen, H. Li, G. Pang, H. Dou and X. Zhang, *Adv. Funct. Mater.*, 2016, **26**, 3703–3710.
7 P. Senguttuvan, G. Rousse, V. Seznec, J.-M. Tarascon and M. R. Palacín, *Chem. Mater.*, 2011, **23**, 4109–4111.
8 L. Zhao, J. Zhao, Y.-S. Hu, H. Li, Z. Zhou, M. Armand and L. Chen, *Adv. Energy Mater.*, 2012, **2**, 962–965.
9 A. Rudola, K. Saravanan, C. W. Mason and P. Balaya, *J. Mater. Chem. A*, 2013, **1**, 2653.
10 Y. Park, D.-S. Shin, S. H. Woo, N. S. Choi, K. H. Shin, S. M. Oh, K. T. Lee and S. Y. Hong, *Adv. Mater.*, 2012, **24**, 3562–3567.
11 H. Pan, X. Lu, X. Yu, Y.-S. Hu, H. Li, X.-Q. Yang and L. Chen, *Adv. Energy Mater.*, 2013, **3**, 1186–1194.
12 J. M. Feckl, K. Fominykh, M. Doblinger, D. Fattakhova-Rohlfing and T. Bein, *Angew. Chem., Int. Ed.*, 2012, **51**, 7459–7463.

13 S. Balendhran, J. Deng, J. Z. Ou, S. Walia, J. Scott, J. Tang, K. L. Wang, M. R. Field, S. Russo, S. Zhuiykov, M. S. Strano, N. Medhekar, S. Sriram, M. Bhaskaran and K. Kalantar-zadeh, *Adv. Mater.*, 2013, **25**, 109–114.

14 X. K. Hu, Y. T. Qian, Z. Song, J. R. Huang, R. Cao and J. Q. Xiao, *Chem. Mater.*, 2008, **20**, 1527–1533.

15 Y. Ding, P. Zhang, Y. Jiang and D. Gao, *Solid State Ionics*, 2007, **178**, 967–971.

16 P. Zhang, Y. Huang, W. Jia, Y. Cai, X. Wang, Y. Guo, D. Jia, Z. Sun and Z. Guo, *Electrochim. Acta*, 2016, **210**, 935–941.

17 G. B. Xu, L. W. Yang, X. L. Wei, J. W. Ding, J. X. Zhong and P. K. Chu, *J. Power Sources*, 2015, **295**, 305–313.

18 Y. Zhang, S. Xia, Y. Zhang, P. Dong, Y. Yan and R. Yang, *Sci. Bull.*, 2012, **57**, 4181–4187.

19 T. Brezesinski, J. Wang, S. H. Tolbert and B. Dunn, *Nat. Mater.*, 2010, **9**, 146–151.

20 H. Wu, G. Zheng, N. Liu, T. J. Carney, Y. Yang and Y. Cui, *Nano Lett.*, 2012, **12**, 904–909.

21 H. Lindström, S. Södergren, A. Solbrand, H. Rensmo, J. Hjelm, A. Hagfeldt and S.-E. Lindquist, *J. Phys. Chem. B*, 1997, **101**, 7717–7722.

22 J. Wang, J. Polleux, J. Lim and B. Dunn, *J. Phys. Chem. C*, 2007, **111**, 14925–14931.

23 V. Augustyn, J. Come, M. A. Lowe, J. W. Kim, P. L. Taberna, S. H. Tolbert, H. D. Abruna, P. Simon and B. Dunn, *Nat. Mater.*, 2013, **12**, 518–522.

24 H. Vogt, *Electrochim. Acta*, 1994, **39**, 1981–1983.

25 F. Ning, B. Xu, J. Shi, M. Wu, Y. Hu and C. Ouyang, *J. Phys. Chem. C*, 2016, **120**, 18428–18434.

26 C. Ouyang, Y. Du, S. Shi and M. Lei, *Phys. Lett. A*, 2009, **373**, 2796–2799.

27 D. Gonbeau, C. Guimon, G. Pfister-Guillouzo, A. Levasseur, G. Meunier and R. Dormoy, *Surf. Sci.*, 1991, **254**, 81–89.

28 H. S. Kim, J. B. Cook, H. Lin, J. S. Ko, S. H. Tolbert, V. Ozolins and B. Dunn, *Nat. Mater.*, 2017, **16**, 454–460.